Assessing the health degree of winter wheat under field conditions for precision plant protection by using UAV imagery

Mengmeng Du[1,2], Zidi Xie[1], Heng Wang[2], Jiangtao Ji[1,2*], Xin Jin[1,2], Ali Roshanianfard[3]

(1. *College of Agricultural Equipment Engineering, Henan University of Science and Technology, Luoyang 471003, Henan, China*;
2. *Longmen Laboratory, Luoyang 471000, Henan, China*;
3. *Department of Agriculture and Natural Resources, University of Mohaghegh Ardabili, 566199 Ardabil, Iran*)

Abstract: Widespread infestation of pests and pathogens during winter wheat's heading stage poses significant risks to yield loss. In this study, an assessment model of health degree (HD) of winter wheat under field conditions was established by using unmanned aerial vehicle remote sensing (UAV RS) imagery. Firstly, non-photosynthetic features were identified from the UAV RS imagery based on different machine learning methods, including Minimum Distance (MD), Maximum Likelihood Estimation (MLE), and Support Vector Machine (SVM). Classification results indicated that MD demonstrates the best performance, according to the values of Overall Accuracy (0.898), Kappa Coefficient (0.863), and Precision (0.856). Therefore, the inversion model between the proportion of pixels classified as non-photosynthetic features and the corresponding ground truth of the incidence of non-photosynthetic features was established. Coefficient of determination (R^2), RMSE (root mean square error), and RRMSE (Relative RMSE) of the inversion model are 0.73, 4.86%, and 19.81%, respectively, demonstrating strong correlation and high accuracy. Subsequently, an assessment model for HD of the wheat field was generated based on the predicted incidence of the non-photosynthetic features, and the conclusion was reached that HD1 (pre-symptoms of the infestation of pests and pathogens) dominated in the wheat field, with the proportion of area as 56.16%, while HD4 and HD5 (severe infestation of pests and pathogens) were negligible, with proportions of area of 2.29% and 17.75%. Finally, the assessment model of HD was used to simulate the precision OSMP (One-Spray-Multiple-Protection), and the agricultural chemical could be reduced to 69.11% of the conventional OSMP operation, which provides theoretical and methodological support for the reduction of agricultural chemicals in the domain of precision agriculture.

Keywords: winter wheat, UAV, remote sensing, pests and pathogens, plant protection, precision agriculture
DOI: 10.25165/j.ijabe.20251803.9226

Citation: Du M M, Xie Z D, Wang H, Ji J T, Jin X, Roshanianfard A. Assessing the health degree of winter wheat under field conditions for precision plant protection by using UAV imagery. Int J Agric & Biol Eng, 2025; 18(3): 195–203.

1 Introduction

Wheat is one of the most important staple cereals in the world[1]. The cultivation acreage of winter wheat (*Triticum aestivum* L.) is about 22 million hm^2 in China, representing 92.5% of the total wheat cultivation[2-4]. During the heading stage of winter wheat, high humidity and increased temperature often lead to infestation of various kinds of pests and pathogens such as wheat aphids (*Sitobion avenae*)[5], stripe rust (*Puccinia Striiformis* F. *Sp. Tritici*.)[6,7], fusarium head blight[8-10], and other plant diseases[11-15], which poses significant risks to yield and grain quality[16-19]. Researchers have found that diseases can decrease annual wheat yields by approximately 5%[20], and Zhang et al. demonstrated that overall wheat yield losses caused by pests and pathogens in the main wheat planting region of the Yellow and Huai River Region was up to 16.29% of the regional yield and has been on the rise[21].

For comprehensive control of pests and pathogens during winter wheat's heading stage, the most common and conventional plant protection practice known as One-Spray-Multiple-Protection (OSMP) is implemented by mixing several kinds of insecticides, fungicides, and growth regulators[22]. Proper conduction of OSMP is based on accurate knowledge of the exact location, extent, and severity of the infestation of pests and pathogens. Traditionally, acquisition of information on pests and pathogens of field crops heavily relied on field surveys through manual rating, which is time-consuming, labor-intensive, and subject to human error[23].

On the other hand, remote sensing (RS) techniques are utilized to monitor crops' growth status by using satellite and airborne RS imagery[24,25]. Studies and applications of RS on pest and disease infestations have traversed over 30 years of history, since Riley[26] pointed out that plant damage could be identified from RS images by detecting the changes of the appearance of plant foliage. During the last four decades, a large number of agricultural RS applications have been put forward, encompassing visual interpretation and quantitative analysis of RS imagery[27-31], as spectral reflectance properties of non-photosynthetic features caused by pests and diseases are significantly different from healthy plants[32].

Mirik et al.[33] identified wheat plants with streak mosaic virus from multispectral satellite RS images by using maximum likelihood classifier at regional level (two adjacent counties), and the overall accuracies were between 89.47 and 99.07%. Römer et al.[34] collected hyperspectral fluorescence data (370-800 nm) of pre-

Received date: 2024-07-15 **Accepted date:** 2025-03-31
Biographies: **Mengmeng Du**, Associate Professor, research interest: smart agricultrure and remote sensing, Email: dualmon.du@haust.edu.cn; **Zidi Xie**, Undergraduate, research interest: agricultural mechanization, Email: 2314300301 46@stu.haust.edu.cn; **Heng Wang**, MS, research interest: agricultural engineering, Email: wanghengvip666@163.com; **Xin Jin**, Professor, research interest: agricultural engineering, Email: jx.771@163.com; **Ali Roshanianfard**, PhD, research interest: agricultural engineering, Email: alirf@uma.ac.ir.
***Corresponding author: Jiangtao Ji**, Professor, research interest: agricultural engineering. Henan University of Science and Technology, No.48 Xiyuan Road, Jianxi District, Luoyang 471003, Henan, China. Tel: +86-538-8241865, Email: jjt0907@163.com.

symptomatic wheat leaf rust and healthy plants in a controlled-environment cabinet, and support vector machines were used for classification with high accuracy of 93%. Zhang et al.[35] detected powdery mildew of winter wheat by measuring hyperspectral reflectance of normal and infected leaves with a spectroradiometer in a laboratory, and associated 32 spectral features with the disease severity by using partial least square regression (R^2=0.80). Zhang et al.[36] investigated the accuracy of detecting wheat yellow rust based on continuous wavelet analysis on hyperspectral data of healthy and infected plants in a laboratory, and results showed that relatively high accuracy levels (R^2=0.72) were maintained at the spectral interval of 16 nm. There have been a handful of other studies that investigated the spectral signatures of wheat plants infected with pests and pathogens, which revealed a great potential of RS techniques in monitoring of wheat growth status[37-42].

Based on the literature review, it seems feasible for most studies to recognize each specific disease by analyzing multispectral or hyperspectral data acquired by using proximal or in-door devices. However, there are also some limitations to using multispectral/hyperspectral devices in monitoring infestations of pests and diseases under field condition. Firstly, hyperspectral data, with hundreds of narrow spectral bands, demand advanced computational resources and expertise for calibration, stitching, and analysis[43]. Deploying UAV (Unmanned Aerial Vehicle) RS systems with these sensors requires trained personnel for flight planning and data capture, which complicates real-time field applications. Furthermore, the measurement of hyperspectral reflectance data requires devices to be held close-range to plants, which thus limits the field of view of cameras and efficiency over vast areas. Besides, the aerodynamic downwash generated by UAV RS systems during low-altitude flight operations induces airflow interactions with vegetation surfaces, resulting in transient modifications to the structural configuration of plant canopy elements and systematic artifacts in hyperspectral reflectance data.

Although Zhang et al.[44] and Qi et al.[45] proposed innovative methods of assessing the severity of fusarium head blight of wheat ears (R^2=0.98) and yellow-leaf disease of rubber trees (R^2=0.82) by using high-resolution digital imagery, to date there have been few studies on the overall severity of pests and pathogens of winter wheat under field condition by using UAV RS digital imagery, which features high efficiency, low cost, and easy deployment.

Therefore, to address the challenges of acquiring information on infestation of pests and pathogens of winter wheat accurately and efficiently, this study explores the utilization of a consumer-level drone of DJI mini 2 to collect digital images of winter wheat at field scale. This study introduces the conception of non-photosynthetic features usually caused by the infestation of pests and diseases during winter wheat's heading stage, and hypothesizes that they can be accurately identified in the UAV RS imagery based on machine learning methods. The main objective is to calculate and evaluate the accuracy of the incidence of non-photosynthetic features from the UAV RS imagery. Subsequently, an assessment model for health degree (HD) of the wheat field can be generated to facilitate the precise implementation of the OSMP. The implementation of the non-contact, high-efficiency, and low-cost UAV RS approach of detecting plant pests and diseases at field scale could greatly advance the progress of the precise OSMP application.

2 Material and methods

2.1 Experimental field

The wheat field under study was located in Luoyang City, Henan province, China, shown in Figure 1. This region has a semi-arid continental monsoon climate, and the average annual precipitation, effective accumulated temperature, and frost-free period are about 578 mm, 4654°C, and 210 days, respectively. The parental soil material is alluvium of the Yellow River, mainly composed of tidal soil with medium fertility. Alkali-hydrolyzable nitrogen content, available phosphorus content, and available potassium content were measured as 57 mg/kg, 13 mg/kg, and 72 mg/kg, respectively, by using a portable soil nutrient meter (Zhengda, Wenzhou, China).

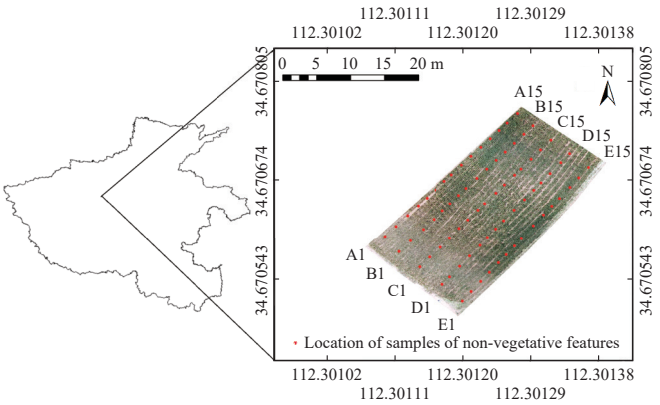

Figure 1 Location of wheat field and distribution of ground truth data

The tested variety of winter wheat was AK-58, and peanut was the previous crop. On 11 October 2023, wheat was sowed with the seeding volume of 165 kg/hm^2 by using an eight-row seeder (Nonghaha, Shijiazhuang, China), of which the row spacing was set to 20 cm. Urea of 46% purity, ammonium phosphate of 61% purity, and potassium chloride of 60% purity were uniformly mixed and used as basal fertilizers at the rate of 225 kg/hm^2 prior to wheat seeding via rotary tillage.

2.2 Acquisition of UAV RS imagery

The UAV RS experiment was conducted on May 10, 2024 during the heading period of winter wheat. UAV RS images were captured around local noon time by using the DJI Mini 2 with a CMOS [Complementary Metal Oxide Semiconductor (Dajiang Innovation, Shenzhen, China)] imaging sensor. Parameters of the UAV platform as well as the CMOS imaging sensor are listed in Table 1.

Table 1 Parameters of the UAV platform and imaging sensor

Equipment	Items	Values
UAV platform	Overall size (mm×mm×mm)	245×289×56
	Net weight/g	249
	Flight altitude/m	30
Imaging sensor	Angle of view/(°)	83
	Type of imager	CMOS
	Effective pixels	3000×4000
	Equivalent focal length/mm	24
	Exposure/s	1/100
	ISO speed	100
	Aperture	2.8
	Image format	JPEG

Flight altitude of UAV was set to 30 m above ground level to acquire visible-band images with high spatial resolution of about 6 mm, which provides a large field-of-view and detailed image

features at the same time. The camera shutter speed and ISO value were set to 1/100 s and 100. As the result, 16 pieces of effective UAV RS images with a longitudinal and lateral overlapping rate of about 70% were acquired in total, which were processed in Agisoft Metashape Professional software (Agisoft LLC, St. Petersburg, Russia) to generate an ortho-mosaic image, also shown in Figure 1, so that the health degree of winter wheat can be assessed at the field scale. The ortho-mosaic image was geo-referenced by measuring the geological coordinates of four field corners as ground controlling points with Real Time Kinematic Global Navigation Satellite System (RTK-GNSS) modules, the overall positioning accuracy of which is about 2 cm.

2.3 Field inspection of non-photosynthetic features

On completion of the UAV RS experiment, wheat tiller number (T_m) within the "1-meter-double-row" area was manually counted. The geological coordinates of each sampling point were also measured by using the RTK-GNSS module, the distribution of which are also shown in Figure 1 as red dots in five rows, from row A to row E.

Since symptoms of various kinds of pests and diseases on infected wheat plants are commonly characterized by chlorotic streaking, lesions, or pustules (non-photosynthetic features) of young leaves[33], the number of young wheat cauline leaves with such non-photosynthetic features (N_m) for each sampling point was acquired by visually inspecting the top five cauline leaves of each individual wheat plant, i.e. the flag-leaf, top second leaf, top third leaf, top fourth leaf, and top fifth leaf. Due to the constraints imposed by manual field inspection and to evaluate the overall health degree of winter wheat under field condition for the facilitation of the OSMP operation, this study does not differentiate the size, quantity, or types of the non-photosynthetic features associated with various kinds of pests and pathogens. And as small non-photosynthetic features are prone to be invisible to the UAV RS system, any occurrence of a mold spot or disease lesion covering 50% or more of the individual wheat cauline leaf area was considered as one counting event, shown in Figure 2 as marked in red lines.

Accordingly, incidence of non-photosynthetic features in wheat plants (R) was calculated as Equation (1) and Equation (2).

$$R = \frac{N_m}{L_m} \times 100\% \tag{1}$$

$$L_m = T_m \times 5 \tag{2}$$

where, R, N_m, L_m, and T_m are the ground truth of incidence of non-photosynthetic features, the numbers of wheat cauline leaves with non-photosynthetic features, total number of wheat cauline leaves, and wheat tiller numbers within the "1-meter-double-row" area around each sampling point, respectively.

Figure 2 Wheat cauline leaf (marked in red lines) with non-photosynthetic features

2.4 Annotating endmembers in UAV RS imagery

In remote sensing imagery, pixels containing only one component are referred to as endmembers, while others containing two or more components are designated as mixed pixels[45-49]. Annotation of endmember pixels in remote sensing imagery is a prerequisite for extracting image features based on supervised machine learning algorithms.

Based on the characteristics and distribution of different features in the UAV RS imagery during the winter wheat heading stage, four kinds of endmembers were manually annotated, including shadow features formed by mutual shading between wheat plants, bare soil features, healthy vegetation, and non-photosynthetic features, shown in Figure 3.

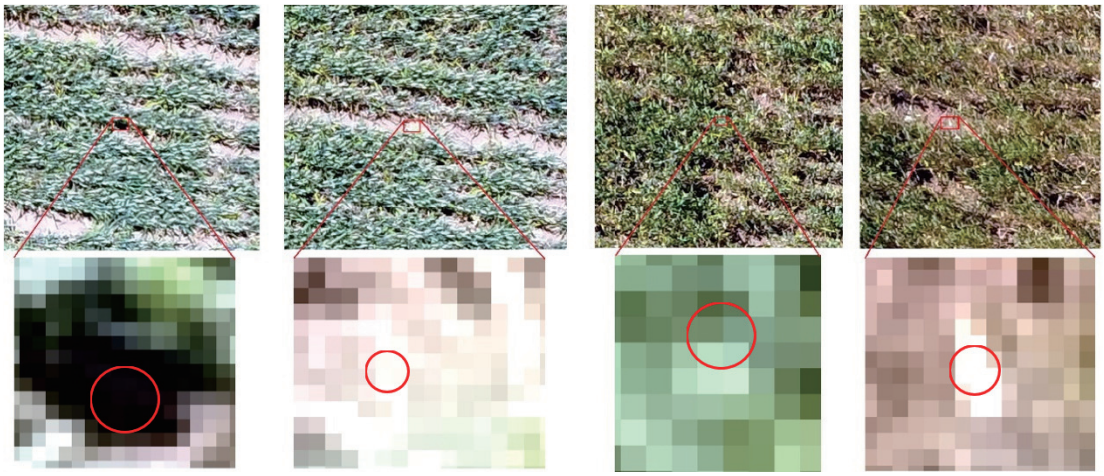

a. Shadow b. Bare soil c. Healthy vegetation d. Non-photosynthetic features

Figure 3 Annotating endmembers

In total, 300 endmembers of shadow, bare soil, healthy vegetation, and non-photosynthetic features were annotated, respectively, which were uniformly distributed throughout the whole wheat field as shown in Figure 4.

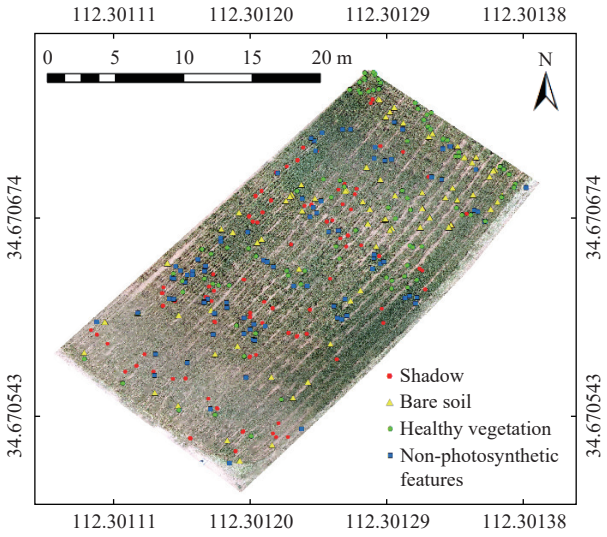

Figure 4 Distribution of annotated endmembers

2.5 Identification and evaluation of non-photosynthetic features

Seventy percent of endmembers were randomly selected as the training dataset and the remaining as the test dataset, and the UAV RS imagery was classified into four categories of shadow, bare soil, healthy vegetation, and non-photosynthetic features, based on machine learning methods.

Supervised classification of remote sensing images refers to the process of identifying pixels of unknown category by using a training set of pixels with confirmed categories. In this study, supervised machine learning algorithms including Minimum Distance (MD), Maximum Likelihood Estimation (MLE), and Support Vector Machine (SVM) were employed to extract the non-photosynthetic features in the UAV RS images, based on the training datasets of endmembers of shadow, bare soil, healthy vegetation, and non-photosynthetic features.

Three parameters of Overall Accuracy (OA), Kappa Coefficient (KC), and Precision (P) were used to evaluate the accuracies of classification results based on MD, MLE, and SVM methods, according to Equations (3) to (6), by using the test dataset of endmembers.

$$\mathrm{OA}=\frac{\mathrm{TP}+\mathrm{TN}}{\mathrm{TP}+\mathrm{FN}+\mathrm{FP}+\mathrm{TN}} \tag{3}$$

$$\mathrm{KC}=\frac{\mathrm{OA}-P_e}{1-P_e} \tag{4}$$

$$P_e=\frac{\sum(a_i\times b_i)}{n^2} \tag{5}$$

$$P=\frac{\mathrm{TP}}{\mathrm{TP}+\mathrm{FP}} \tag{6}$$

where, TP, TN, FN, and FP denote true positive samples, true negative samples, false negative samples, and false positive samples, respectively; P_e, a_i, b_i, and n denote an intermediate variable for calculating KC value, the number of pixels for each category in the test set, the number of pixels for each category of the classified results, and the total number of pixels in the test set, respectively.

2.6 Health degree of winter wheat

As the wheat stripe rust is among the high-incidence diseases during winter wheat's heading stage, according to Chinese Standard GB/T 15795-2011 "Rules for monitoring and forecast of the wheat stripe rust (*Puccinia striiformis* West)", health degree (HD) of winter wheat is categorized into five scales according to the incidence of non-photosynthetic features around each sampling area (Table 2). HD1 indicates the pre-symptoms of the infestation of pests and pathogens, as the incidence of non-photosynthetic features is very low; this is suggested to be sprayed with the least dosage of agricultural chemicals. HD5 represents the most severe scenario of the infestation of pests and pathogens, and increased dosages of agricultural chemicals are preferable for the effective control of pests and pathogens.

Table 2 Health degree of winter wheat

Health degree (HD)	Incidence of non-photosynthetic features (x)
1	0.001%<x≤5%
2	5%<x≤10%
3	10%<x≤20%
4	20%<x≤30%
5	30%<x≤100%

2.7 Simulation of precision OSMP

Variable-rate prescription for the precision OSMP was established according to the HD model of the wheat field. The prescription applied the conventional dosage of the OSMP to the areas of HD3, while one-third, two-thirds, four-thirds, and five-thirds of the conventional dosage were applied to the areas of HD1, HD2, HD4, and HD5, respectively, according to the following model:

$$\mathrm{Do}=\begin{cases}1/3\mathrm{Do_{co}}, & \text{if } I\in[0,0.1]\\ 2/3\mathrm{Do_{co}}, & \text{if } I\in[0.11,0.3]\\ \mathrm{Do_{co}}, & \text{if } I\in[0.31,0.5]\\ 4/3\mathrm{Do_{co}}, & \text{if } I\in[0.51,0.7]\\ 5/3\mathrm{Do_{co}}, & \text{if } I\in[0.71,1]\end{cases} \tag{7}$$

where, Do, $\mathrm{Do_{co}}$, and I indicate the variable-rate dosage for the precision OSMP, L; the conventional dosage used in the region, L; and the incidence of non-photosynthetic features.

3 Results and discussion

3.1 Ground truth of incidence for non-photosynthetic features

Wheat tiller numbers within the "1-meter-double-row" area (T_m) were manually counted and listed in Table 3.

Table 3 Wheat tiller numbers within the "1-meter-double-row" area

Serial No.	Row mark				
	A	B	C	D	E
1	16	21	21	19	31
2	18	21	27	38	16
3	11	22	15	23	22
4	10	12	18	15	36
5	11	12	14	10	45
6	5	73	22	7	56
7	17	55	45	21	79
8	40	43	38	47	102
9	36	40	36	45	108
10	40	67	31	73	103
11	56	67	31	20	79
12	56	49	34	23	65
13	67	65	51	18	58
14	80	31	35	47	31
15	22	4	6	22	20

According to Equation (2), total numbers of wheat cauline leaves (L_m) were calculated. Based on the numbers of wheat cauline leaves with non-photosynthetic features, which were manually inspected in the wheat field as mentioned in Section 2.3 and listed in Table 4, the intensities of non-photosynthetic features' ground truth data around each sampling area were calculated according to Equation (1) and are listed in Table 5.

Table 4 Numbers of wheat cauline leaves with non-photosynthetic features

Serial No.	Row mark				
	A	B	C	D	E
1	23	19	59	23	90
2	26	15	39	62	7
3	14	22	6	16	17
4	6	12	13	9	10
5	9	11	24	4	25
6	6	36	42	6	18
7	16	68	80	34	29
8	49	56	23	108	90
9	34	115	73	120	78
10	132	140	68	132	54
11	125	82	49	37	139
12	35	19	18	38	58
13	68	52	36	24	42
14	83	38	34	86	14
15	20	6	10	14	49

Table 5 Intensity of non-photosynthetic features' ground truth data

Serial No.	Row mark				
	A	B	C	D	E
1	28.75%	18.10%	56.19%	24.21%	58.06%
2	28.89%	14.29%	28.89%	32.63%	8.75%
3	25.45%	20.00%	8.00%	13.91%	15.45%
4	12.00%	20.00%	14.44%	12.00%	5.56%
5	16.36%	18.33%	34.29%	8.00%	11.11%
6	24.00%	9.86%	38.18%	17.14%	6.43%
7	18.82%	24.73%	35.56%	32.38%	7.34%
8	24.50%	26.05%	12.11%	45.96%	17.65%
9	18.89%	57.50%	40.56%	53.33%	14.44%
10	66.00%	41.79%	43.87%	36.16%	10.49%
11	44.64%	24.48%	31.61%	37.00%	35.19%
12	12.50%	7.76%	10.59%	33.04%	17.85%
13	20.30%	16.00%	14.12%	26.67%	14.48%
14	20.75%	24.52%	19.43%	36.60%	9.03%
15	18.18%	30.00%	33.33%	12.73%	49.00%

From Table 5, the intensity of non-photosynthetic features' ground truth data varies from 5.56% to 66.00%, while the average and standard deviations are 24.76% and 14.07%, respectively. It could be concluded that the health degree of this experimental wheat field is from HD2 to HD5, indicating slight to severe symptoms. However, the discrete point-source sampling data of field survey cannot truthfully reflect the details of the overall infestation of pests and pathogens in the wheat field, which needs further processing in combination with the UAV RS imagery.

3.2 Classification results of UAV RS imagery

According to the endmembers of shadow, bare soil, healthy vegetation, and non-photosynthetic features in Section 2.4, the spectral signatures of each kind of endmember were extracted and are shown in Figure 5.

Figure 5 illustrates the spectral signatures of different kinds of endmembers. Non-photosynthetic vegetation features showed the highest reflectance regardless of the blue, green, and red band in the UAV RS imagery, when compared with bare soil, healthy vegetation, and shadow. The result complies with previous studies of Cheng et al.[50] and Feng et al[51], which demonstrated that infected plants showed an increase in the corresponding optical reflectance for different crops and diseases. It can also be verified in the previous research that the reflectance of healthy vegetation is far less than that of the bare soil in each spectral band[13]. However, it can also be noticed that the spectral responses of non-photosynthetic features and bare soil are similar, which could pose a certain risk of inaccuracy in differentiating these two classes by using machine learning methods. On the other hand, healthy vegetation and non-photosynthetic features exhibit significant difference, indicating ideal characteristics of features to be separated, which provides theoretical basis for implementing precise plant protection based on the extraction of non-photosynthetic features.

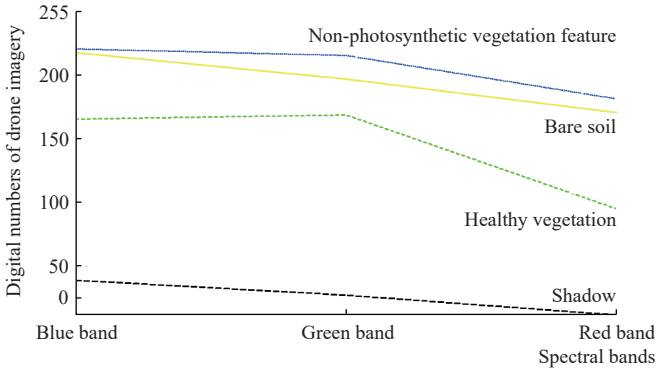

Figure 5 Spectral signatures of different kinds of endmembers

According to the training dataset in Section 2.4, the UAV RS imagery was classified into four categories of shadow, bare soil, healthy vegetation, and non-photosynthetic features, based on the machine learning methods of MD, MLE, and SVM, respectively. The classification results are shown in Figure 6.

From the statistics of the classification results in Table 6, it could be concluded that the proportion of pixels classified as shadow using the MD method is significantly higher than the classification results obtained by MLE and SVM. On the other hand, the proportion of pixels identified as non-photosynthetic features is lower than the latter two. However, there is no significant difference in the proportion of pixels belonging to the categories of healthy vegetation and bare soil features. The accuracy of the classification results is to be validated in Section 3.3.

Table 6 Proportion of pixels classified as different categories

Categories	Percentage		
	MD	MLE	SVM
Shadow	12.31%	5.82%	7.57%
Bare soil	4.96%	4.95%	6.00%
Healthy vegetation	27.57%	28.21%	27.06%
Non-photosynthetic features	55.16%	61.02%	59.37%
Sum	100.00%	100.00%	100.00%

3.3 Validating classification accuracy of UAV RS imagery

To validate the classification accuracy, confusion matrices were computed for the supervised classification algorithms based on the test dataset. The results are presented in Table 7.

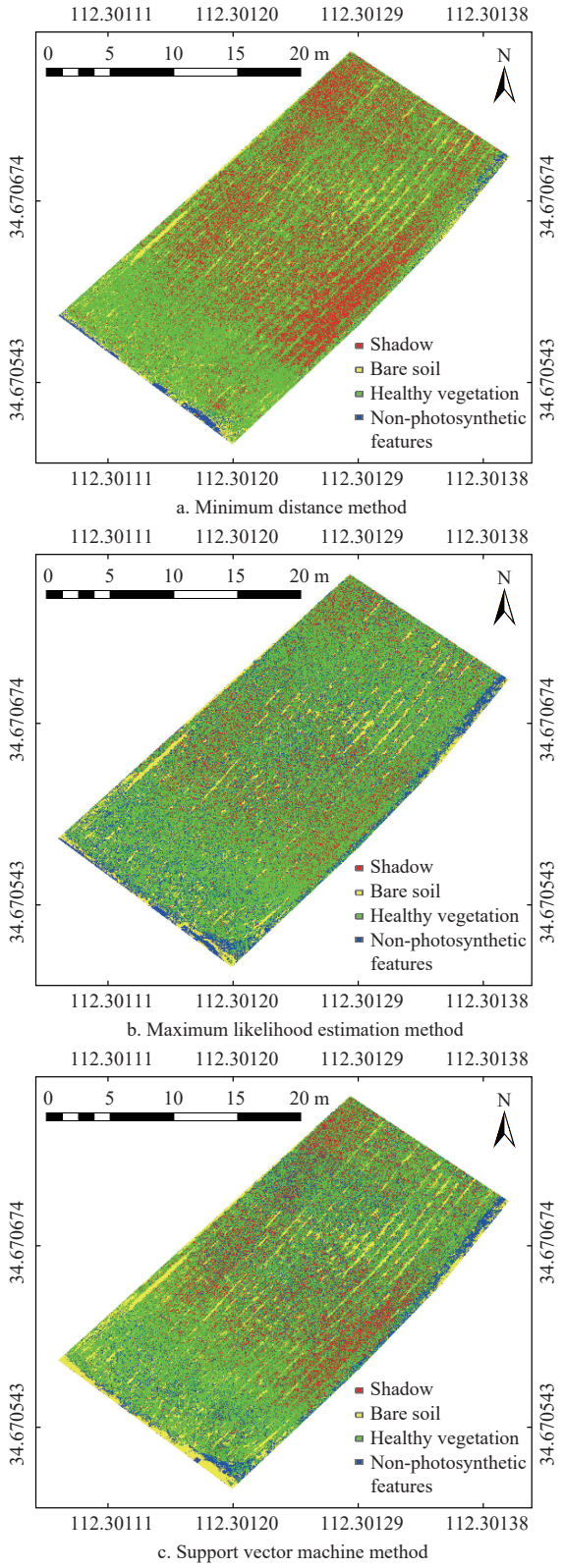

Figure 6 Classification results based on the three different machine learning methods

According to Equation (3) and Table 7, OA of the classification results based on MD, MLE, and SVM were calculated as 0.898, 0.83, and 0.853, respectively. Besides, KC of the classification results based on MD, MLE, and SVM were calculated as 0.863, 0.773, and 0.803, respectively, according to Equations (4)-(5) and Table 5. *P* of the classification results based on MD, MLE, and SVM were calculated as 0.856, 0.711, and 0.736, respectively, according to Equation (6) and Table 5. Therefore, MD demonstrates the best performance in extracting non-photosynthetic features from the UAV RS imagery of winter wheat at the heading stage, based on the values of Overall Accuracy, Kappa Coefficient, and Precision.

Table 7 Confusion matrices of different supervised classification methods

Categories	MD				
	Bare soil	Healthy vegetation	Shadow	Non-photosynthetic features	Sum
Bare soil	88	6	1	14	109
Healthy vegetation	0	88	0	2	90
Shadow	0	4	99	0	103
Non-photosynthetic features	12	2	0	84	98
Sum	100	100	100	100	400
Categories	MLE				
	Bare soil	Healthy vegetation	Shadow	Non-photosynthetic features	Sum
Bare soil	95	0	0	31	126
Healthy vegetation	0	84	0	15	99
Shadow	0	0	99	0	99
Non-photosynthetic features	5	16	1	54	76
Sum	100	100	100	100	400
Categories	SVM				
	Bare soil	Healthy vegetation	Shadow	Non-photosynthetic features	Sum
Bare soil	94	0	0	34	128
Healthy vegetation	0	84	0	2	86
Shadow	0	0	99	0	99
Non-photosynthetic features	6	16	1	64	87
Sum	100	100	100	100	400

The MD classifier assigns a group of pixels to the pre-trained class whose mean vector is closest in the feature space (spectral response in this paper). It uses Euclidean distance as a measure of proximity and is particularly effective when the distance between class means is large, such as distinguishing objects of different types based on spectral signatures[52]. By analyzing spectral deviations, the MD classifier can detect anomalies in healthy vegetation, which explains its high accuracy in differentiating non-photosynthetic features from healthy vegetation in this paper. However, it should also be acknowledged that classification accuracy is highly dependent on the quality of prepared training data, which defines how classes are represented in the feature space. Poor-quality data (e.g., mislabeled pixels, few samples, incomplete classes) distorts these representations, leading to biased models and reduced performance.

3.4 Inverting incidence of non-photosynthetic features

From Section 3.3, this study reached the conclusion that the classification result of the MD method has high accuracy in identifying non-photosynthetic features from the UAV RS imagery. Therefore, the incidence of non-photosynthetic features over the total pixels of each sampling point of "1-meter-double-row" area was acquired, based on the classification result of the MD method (Figure 6a), listed in Table 8.

From the intensity of non-photosynthetic features' ground truth data acquired by manual inspection (Table 5) and the incidence of non-photosynthetic features in the UAV RS imagery, the inversion model was established, as seen in Figure 7, by randomly selecting 50 sets of data from Table 5 and Table 8 as training data. The coefficient of determination (R^2) is 0.73, which indicates a good

correlation between incidence of non-photosynthetic features in the UAV RS imagery and the intensity of non-photosynthetic features' ground truth data.

Table 8 Incidence of non-photosynthetic features

Serial No.	Row mark				
	A	B	C	D	E
1	1.18%	0.63%	2.16%	0.99%	3.25%
2	0.35%	0.54%	0.65%	0.89%	0.10%
3	1.05%	0.14%	0.27%	0.29%	0.17%
4	0.42%	0.73%	0.53%	0.38%	0.10%
5	0.60%	0.66%	0.64%	0.52%	0.11%
6	1.44%	0.88%	1.61%	0.68%	0.06%
7	0.72%	0.81%	1.55%	1.35%	0.01%
8	0.79%	0.82%	0.93%	1.80%	0.04%
9	0.75%	2.90%	1.39%	2.23%	0.04%
10	4.38%	1.47%	1.78%	2.46%	0.43%
11	1.97%	1.00%	1.15%	1.32%	1.02%
12	0.33%	0.11%	0.67%	1.45%	0.60%
13	0.50%	0.78%	0.45%	1.41%	0.40%
14	0.48%	0.68%	0.34%	1.24%	0.24%
15	0.68%	2.13%	1.32%	0.73%	1.90%

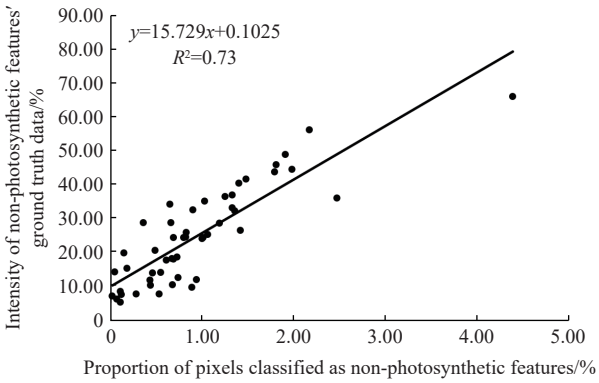

Note: x and y denote the incidence of non-photosynthetic features in the UAV RS imagery and the intensity of non-photosynthetic features' ground truth data, respectively; while R^2 is the coefficient of determination.

Figure 7 Inversion model of incidence of non-photosynthetic features

3.5 Evaluating accuracy of the inversion model

To evaluate the accuracy of the inversion model mentioned in Section 3.4, the remaining 25 sets of data from Table 5 and Table 8 were used as validating data, listed in Table 9.

The predicted incidence of non-photosynthetic features was calculated according to the inversion model of Section 3.4. The corresponding intensities of non-photosynthetic features' ground truth data are also listed in Table 9. Consequently, the RMSE (root mean square error) and RRMSE (Relative RMSE) of the inversion model were calculated as 4.86% and 19.81%, respectively, which shows high accuracy and indicates the feasibility of predicting the incidence of non-photosynthetic features based on UAV RS imagery.

3.6 Health degree model of winter wheat

According to the classification result of the MD method in Section 3.2 and the inversion model in Section 3.4, the incidence of non-photosynthetic features was predicted for the experimental field. Subsequently, to facilitate the OSMP operation, the assessment model of the HD of wheat field was generated based on Table 2 in Section 2.6, by averaging the predicted incidence of non-photosynthetic features within the areas of about 1×1 meter (local window of 165×165 pixels), as shown in Figure 8.

Table 9 Validating data used to evaluate the accuracy of the inversion model

Serial No.	Incidence of non-photosynthetic features	Predicted incidence of non-photosynthetic features	Ground truth data of intensity of non-photosynthetic features
A5	0.60%	19.69%	16.36%
A6	1.44%	32.90%	24.00%
A9	0.75%	22.05%	18.89%
A12	0.33%	15.44%	12.50%
A13	0.50%	18.11%	20.30%
B1	0.63%	20.16%	18.10%
B4	0.73%	21.73%	20.00%
B9	2.90%	55.86%	57.50%
B13	0.78%	22.52%	16.00%
B15	2.13%	43.75%	30.00%
C4	0.53%	18.59%	14.44%
C6	1.61%	35.57%	38.18%
C7	1.55%	34.63%	35.56%
C11	1.15%	28.34%	31.61%
C14	0.34%	15.60%	19.43%
D3	0.29%	14.81%	13.91%
D4	0.38%	16.23%	12.00%
D6	0.68%	20.95%	17.14%
D9	2.23%	45.33%	53.33%
D12	1.45%	33.06%	33.04%
E1	3.25%	61.37%	58.06%
E5	0.11%	11.98%	11.11%
E8	0.04%	10.88%	17.65%
E13	0.40%	16.54%	14.48%
E14	0.24%	14.02%	9.03%

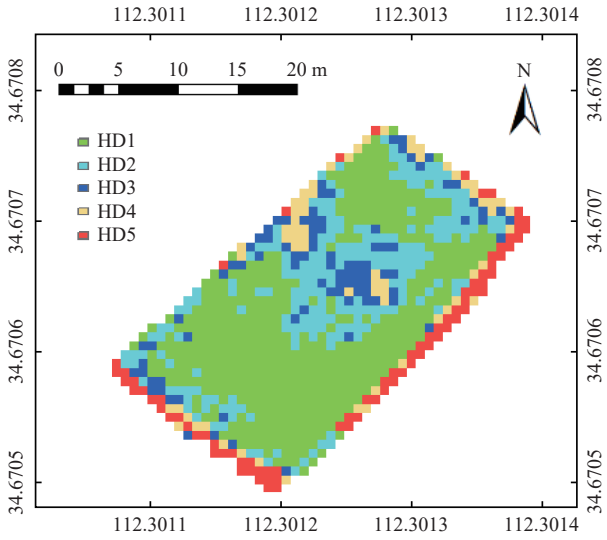

Note: HD1-5 indicates each scale of the health degree (HD) of the wheat field, where HD1, HD2, HD3, HD4, and HD5 represent the predicted incidence of non-photosynthetic features of 0.001-5%, 5-10%, 10-20%, 20-30%, and 30-100%, respectively.

Figure 8 Health degree (HD) model of wheat field

From Figure 8, the percentages of each of the areas of HD1, HD2, HD3, HD4, and HD5 over the total acreage of the experimental field were calculated as 56.16%, 17.92%, 5.88%, 2.29%, and 17.75%, respectively. The conclusion could be reached

that the areas of HD1 (pre-symptoms of infestation of pests and pathogens) dominated in the wheat field, which need less agricultural chemicals in the perspective of precision agriculture. On the other hand, areas of HD4 and HD5 (severe infestation of pests and pathogens) were mostly located alongside field boundaries. As a result, the agricultural chemical could be reduced to 69.11% of the conventional OSMP operation, according to HD model of the wheat field and the simulation model of the precision OSMP.

The aim of this study was to evaluate the potential of machine learning algorithms applied to detecting non-photosynthetic features from UAV RS imagery. The performance of these algorithms was evaluated using parameters of Overall Accuracy, Kappa Coefficient, and Precision. The MD algorithm demonstrated superior performance, with an Overall Accuracy of 0.898, a Kappa Coefficient of 0.863, and a Precision of 0.856. This highlights the importance of selecting appropriate machine learning models for remote sensing applications and suggests that the MD algorithm can be particularly effective in identifying non-photosynthetic features under field condition. This study also presented a practical approach of establishing an HD model at field level, as non-photosynthetic features usually caused by the infestation of pests and diseases during winter wheat's heading stage. The methodology offers a rapid and effective solution for precision plant protection in agriculture.

On the other hand, this study acknowledges that the similarities of spectral signatures between non-photosynthetic features and bare soil (Figure 5) may lead to classification errors. This highlights the complexity of remote sensing applications in agriculture, where environmental factors and the physiological responses of plants can vary significantly. Another limitation is the lack of differentiation between the size, quantity, and type of non-photosynthetic features during manual field inspections. This simplification could potentially affect the accuracy of the regression model for predicting the incidence of non-photosynthetic features.

4 Conclusion

This study developed a rapid approach of assessing health degree (HD) for winter wheat under field conditions for precision plant protection. The approach utilized a light-weight unmanned aerial vehicle (UAV) to collect low-altitude remote sensing (RS) images of the wheat field, and machine learning models were used to identify the non-photosynthetic features from the UAV RS imagery. The main conclusions are summarized as follows:

1) Supervised machine learning algorithms including Minimum Distance (MD), Maximum Likelihood Estimation (MLE), and Support Vector Machine (SVM) were employed to identify non-photosynthetic features in the UAV imagery. MD demonstrates the best performance, based on the values of Overall Accuracy (0.898), Kappa Coefficient (0.863), and Precision (0.856).

2) Based on the classification result of the UAV RS imagery by using MD method, the proportion of pixels classified as non-photosynthetic features was calculated. Subsequently, the linear inversion model between it and the corresponding ground truth of incidence of non-photosynthetic features was established, and the coefficient of determination (R^2) is 0.73, demonstrating strong correlation. The RMSE (root mean square error) and RRMSE (Relative RMSE) of the inversion model were calculated as 4.86% and 19.81%, respectively, which guaranteed high accuracy of inverting the incidence of non-photosynthetic features from the UAV RS imagery.

3) The assessment model of the HD for wheat field was established, and the percentage of each HD scale over the total acreage of the experimental field was calculated. The conclusion was reached that HD1 (pre-symptoms of infestation of pests and pathogens) dominated in the wheat field, with the proportion of area as 56.16%. Finally, simulation of the precision OSMP (One-Spray-Multiple-Protection) was conducted according to the HD model of the wheat field, and the agricultural chemical could be reduced to 69.11% of the conventional OSMP operation. Further studies should explore the applicability of this method to additional relevant wheat species, and verify its effectiveness in wheat fields where different levels of infestation of pests and pathogens occur.

Acknowledgements

This research was jointly funded by the Major Science and Technology Projects of Longmen Laboratory (Grant No. 231100220200) and the National Key Research and Development Program of China (Grant No. 2019YFE0125500-03).

[References]

[1] Zhang Z, Zhang Y L, Shi Y, Yu Z W. Optimized split nitrogen fertilizer increase photosynthesis, grain yield, nitrogen use efficiency and water use efficiency under water-saving irrigation. Scientific Reports, 2020; 10(1): 20310.

[2] National Bureau of Statistics. Statistics on wheat production [DB/OL]. 2023; Available: https://www.gov.cn/lianbo/bumen/202307/content_6892112.htm. Accessed on: [2024-05-16].

[3] Feng Y B, Zhao X S, Li J C, Yu H L, Zhao H P, Yin B Z. Parameter optimization and experiment of the negative pressure precision seed-metering device for wheat. Int J Agric & Biol Eng, 2024; 17(1): 154–162.

[4] Du M M, Roshanianfard A, Liu Y C. Inversion of wheat tiller density based on visible-band images of drone. Spectroscopy and Spectral Analysis, 2021; 41(12): 3828–3836. (in Chinese)

[5] Liu F H, Kang Z W, Tan X L, Fan Y L, Tian H G, Liu T X. Physiology and defense responses of wheat to the infestation of different cereal aphids. Journal of Integrative Agriculture, 2020; 19(6): 1464–1474.

[6] Kiani T, Mehboob F, Hyder M, Zainy Z, Xu L, Huang L, et al. Control of stripe rust of wheat using indigenous endophytic bacteria at seedling and adult plant stage. Scientific Reports, 2021; 11(1): 14473.

[7] Khushboo S S, Gupta V, Pandit D, Abrol S, Choskit D, Farooq S, et al. Epidemiology of stripe rust of wheat: A review. Int J Curr Microbiol App.Sci, 2021; 10(1): 1158–1172.

[8] Wang B, Meng T, Xiao B, Yu T Y, Yue T Y, Jin Y L, et al. Fighting wheat powdery mildew: From genes to fields. Theoretical and Applied Genetics, 2023; 136(9): 196.

[9] Pietrusińska A, Tratwal A. Characteristics of powdery mildew and its importance for wheat grown in Poland. Plant Protection Science, 2020; 56(3): 141–153.

[10] Sakr N, Kurdali F. Silicon root application to manage Fusarium head blight in wheat under field conditions. Gesunde Pflanzen, 2023; 75(2): 261–269.

[11] Rodrighero M B, Fávero C E, Lopes R C, Zielinski A, Granato D, Demiate I M. Wheat technological quality as affected by nitrogen fertilization under a no-till system. Acta Scientiarum Technology, 2015; 37(1): 175–181.

[12] Shewry P R, Hey S J. The contribution of wheat to human diet and health. Food and Energy Security, 2015; 4(3): 178–202.

[13] Du M M, Li M Z, Noguchi N, Ji J T, Ye M C. Retrieval of fractional vegetation cover from remote sensing image of unmanned aerial vehicle based on mixed pixel decomposition method. Drones, 2023; 7(1): 43.

[14] Qiu B W, Luo Y H, Tang Z H, Chen C C, Lu D F, Huang H Y, et al. Winter wheat mapping combining variations before and after estimated heading dates. ISPRS Journal of Photogrammetry and Remote Sensing, 2017; 123: 35–46.

[15] Walsh O S, Klatt A R, Solie J B, Godsey C B, Raun W R. Use of soil moisture data for refined GreenSeeker sensor based nitrogen recommendations in winter wheat (*Triticum aestivum* L.). Precision Agric, 2013; 14: 343–356.

[16] Li T, Yang G Q, Li Q, Jiang Y L, Kang D M, Fan Z Y, et al. Population dynamics of migrant wheat aphids in China's main wheat production

region and their interactions with bacterial symbionts. Frontiers in Plant Science, 2023; 14: 1103236.
[17] Chen X M. Pathogens which threaten food security: Puccinia striiformis, the wheat stripe rust pathogen. Food Security, 2020; 12(2): 239–251.
[18] Buerstmayr M, Steiner B, Buerstmayr H. Breeding for Fusarium head blight resistance in wheat - Progress and challenges. Plant breeding, 2020; 139(3): 429–454.
[19] Goswami R S, Kistler H C. Heading for disaster: Fusarium graminearum on cereal crops. Molecular Plant Pathology, 2004; 5(6): 515–525.
[20] French R C, Stenger D C. Evolution of Wheat streak mosaic virus: Dynamics of population growth within plants may explain limited variation. Annu. Rev. Phytopathol, 2003; 41: 199–214.
[21] Zhang Q Q, Men X Y, Hui C, Ge F, Ouyang F. Wheat yield losses from pests and pathogens in China. Agriculture, Ecosystems & Environment, 2022; 326: 107821.
[22] Chen H B, Lan Y B, Fritz B K, Hoffmann W C, Liu S B. Review of agricultural spraying technologies for plant protection using unmanned aerial vehicle (UAV). Int J Agric & Biol Eng, 2021; 14(1): 38–49.
[23] Abdullah H M, Mohana N T, Khan B M, Ahmed S M, Hossain M, Shakibul Islam K H, et al. Present and future scopes and challenges of plant pest and disease (P&D monitoring: Remote sensing, image processing, and artificial intelligence perspectives. Remote Sensing Applications: Society and Environment, 2023; 32: 100996.
[24] Mulla D J. Twenty five years of remote sensing in precision agriculture: Key advances and remaining knowledge gaps. Biosystems Engineering, 2013; 114(4): 358–371.
[25] Zhang J C, Huang Y B, Pu R L, Gonzalez-Moreno P, Yuan L, Wu K H, et al. Monitoring plant pathogens and pests through remote sensing technology: A review. Computers and Electronics in Agriculture, 2019; 165: 104943.
[26] Riley J R. Remote Sensing in Entomology. Annu. Rev. Entomol, 1989; 34: 247–271.
[27] Chaerle L, Van Der Straeten D. Imaging techniques and the early detection of plant stress. Trends Plant Sci, 2000; 5(11): 495–501.
[28] Ji R, Xie B Y, Li D M, Li Z, Zhang X. Use of MODIS data to monitor the oriental migratory locust plague. Agr. Ecosyst Environ, 2004; 104: 615–620.
[29] Berdugo C A, Mahlein A K, Steiner U, Dehne H W, Oerke E C. Sensors and imaging techniques for the assessment of the delay of wheat senescence induced by fungicides. Fuct Plant Biol, 2013; 40(7): 677–689.
[30] Adelabu S, Mutanga O, Adam E. Evaluating the impact of red-edge band from Rapideye image for classifying insect defoliation levels. ISPRS J Photogramm Remote Sens, 2014; 95: 34–41.
[31] Khanal S, KC K, Fulton J, Shearer S, Ozkan E. Remote sensing in agriculture - accomplishments, limitations, and opportunities. Remote Sens, 2020; 12(22): 3783.
[32] Bauriegel E, Giebel A, Geyer M, Schmidt U, Herppich W B. Early detection of Fusarium infection in wheat using hyper-spectral imaging. Comput Electron Agr, 2011; 75(2): 304–312.
[33] Mirik M, Jones D C, Price J A, Workneh F, Ansley R J, Rush C M. Satellite remote sensing of wheat infected by Wheat streak mosaic virus. Plant Dis, 2011; 95(1): 4–12.
[34] Christoph R, Kathrin B, Mauricio H, Till R, Georg N, Lutz P. Robust fitting of fluorescence spectra for pre-symptomatic wheat leaf rust detection with Support Vector Machines. Computers and Electronics in Agriculture, 2011; 79(2): 180–188.
[35] Zhang J C, Pu R L, Wang J H, Huang W J, Yuan L, Luo J H. Detecting powdery mildew of winter wheat using leaf level hyperspectral measurements. Computers and Electronics in Agriculture, 2012; 85: 13–23.
[36] Zhang J C, Wang B, Zhang X X, Liu P, Dong Y Y, Wu K H, et al. Impact of spectral interval on wavelet features for detecting wheat yellow rust with hyperspectral data. Int J Agric & Biol Eng, 2018; 11(6): 138–144.
[37] Alisaac E, Behmann J, Kuska M T, Dehne H W, Mahlein A K. Hyperspectral quantification of wheat resistance to Fusarium head blight: Comparison of two Fusarium species. European Journal of Plant Pathology, 2018; 152: 869–884
[38] McConachie R, Belot C, Serajazari M, Booker H, Sulik J. Estimating Fusarium head blight severity in winter wheat using deep learning and a spectral index. The Plant Phenome Journal, 2024; 7: e20103.
[39] Zhao J L, Du S Z, Huang L S. Monitoring wheat powdery mildew (Blumeria graminis f. sp. tritici) using multisource and multitemporal satellite images and support vector machine classifier. Smart Agriculture, 2022; 4(1): 17–28. (in Chinese).
[40] Su B F, Liu Y L, Huang Y C, Wei R, Cao X F, Han D J. Analysis for stripe rust dynamics in wheat population using UAV remote sensing. Transactions of the CSAE, 2021; 37(23): 127–135. (in Chinese)
[41] Huang W J, Luo J H, Guan Q S, Zhao J L, Zhang J C. Discriminating wheat aphid damage level using spectral correlation simulating analysis. In: 2013 IEEE International Geoscience and Remote Sensing Symposium – IGARSS, Melbourne, VIC, Australia: IEEE, 2013; pp.3722–3725. doi: 10.1109/IGARSS.2013.6723639.
[42] Luo J H, Huang W J, Yuan L, Zhao C J, Du S Z, Zhang J C, et al. Evaluation of spectral indices and continuous wavelet analysis to quantify aphid infestation in wheat. Precision Agriculture, 2013; 14(2): 151–161.
[43] Barreto A, Reifenrath L, Vogg R, Sinz F, Mahlein A-K. Data augmentation for mask-based leaf segmentation of UAV-images as a basis to extract leaf-based phenotyping parameters. KI - Künstliche Intelligenz, 2023; 37: 143–156.
[44] Zhang D Y, Wang Z C, Jin N, Gu C Y, Chen Y, Huang Y. Evaluation of efficacy of fungicides for control of wheat fusarium head blight based on digital imaging. IEEE Access, 2020; 8: 109876–109890.
[45] Qi J T, Li M, Zhang H M, Zeng T W. Detection of the yellow-leaf disease of rubber trees using low-altitude digital imagery from UAV. Int J Agric & Biol Eng, 2024; 17(6): 245–255.
[46] Chen X, Wang D W, Chen J, Wang C, Shen M G. The mixed pixel effect in land surface phenology: A simulation study. Remote Sensing of Environment, 2018; 211: 338–344.
[47] Jones G, Sirault R. Scaling of thermal images at different spatial resolution: The mixed pixel problem. Agronomy, 2014; 4: 380–396.
[48] Mani P, Rajendiran S, Aruldoss K, Elanchezhian G. Mixed pixel removal in north Tamil Nadu Region for accurate area measurement. Computational Intelligence, 2021; 37(3): 975–994.
[49] Rauf U, Qureshi S W, Jabbar H, Zeb A, Mirza A, Alanazi E, et al. A new method for pixel classification for rice variety identification using spectral and time series data from Sentinel-2 satellite imagery. Computers and Electronics in Agriculture, 2022; 193: 106731.
[50] Cheng T, Rivard B, Sánchez-Azofeifa G A, Feng J, Calvo-Polanco M. Continuous wavelet analysis for the detection of green attack damage due to mountain pine beetle infestation. Remote Sensing of Environment, 2010; 114(4): 899–910.
[51] Feng W, Shen W Y, He L, Duan J Z, Guo B B, Li Y X, et al. Improved remote sensing detection of wheat powdery mildew using dual-green vegetation indices. Precision Agric, 2016; 17: 608–627.
[52] Didore V A, Vaidya R B, Nalawade D, Kale K. Classification of EO-1 Hyperion data using supervised minimum distance algorithm and spectral angle mapper. Journal of Emerging Technologies and Innovative Research, 2021; 8(10): 148–152.